REPORT

CHEMICAL PHYSICS

Coherent imaging of an attosecond electron wave packet

D. M. Villeneuve,[1,2]* Paul Hockett,[1] M. J. J. Vrakking,[3,4] Hiromichi Niikura[5]*

Electrons detached from atoms or molecules by photoionization carry information about the quantum state from which they originate, as well as the continuum states into which they are released. Generally, the photoelectron momentum distribution is composed of a coherent sum of angular momentum components, each with an amplitude and phase. Here we show, by using photoionization of neon, that a train of attosecond pulses synchronized with an infrared laser field can be used to disentangle these angular momentum components. Two-color, two-photon ionization via a Stark-shifted intermediate state creates an almost pure f-wave with a magnetic quantum number of zero. Interference of the f-wave with a spherically symmetric s-wave provides a holographic reference that enables phase-resolved imaging of the f-wave.

In the Copenhagen interpretation of quantum mechanics, a particle is fully described by its complex wave function Ψ, which is characterized by both an amplitude and phase. However, only the square modulus of the wave function, $|\Psi|^2$, can be directly observed (*1*, *2*). Recent developments in attosecond technology based on electron-ion recollision (*3*) have provided experimental tools for the imaging of the electronic wave function (not its square) in bound states or ionization continua. High-harmonic spectroscopy on aligned molecules was used to reconstruct the highest-occupied molecular orbital of nitrogen (*4*, *5*) and to observe charge migration (*6*). Strong-field tunneling was used to measure the square modulus of the highest-occupied molecular orbital for selected molecules (*7*). Furthermore, recollision holography (*8*, *9*) permitted a measurement of the phase and amplitude of a continuum electron generated in an intense laser field.

Complementary to recollision-based measurements, photoelectron spectroscopy with attosecond extreme ultraviolet (XUV) pulses has also measured photoelectron wave packets in continuum states (*10*–*16*) by exploiting quantum interferences (*17*–*19*). However, decomposition of the wave function of an ejected photoelectron into angular momentum eigenstates with a fully characterized amplitude and phase is more difficult. First, in general, a one-photon transition with linearly polarized light generates two orbital angular momentum (ℓ) states, according to the selection rule $\Delta\ell = \pm 1$. Second, because the initial state has a $(2\ell + 1)$-fold degeneracy (labeled by m, the magnetic quantum number) and because m is conserved for interactions with linearly polarized light, photoelectron waves with a range of m are produced. Hence, the photoelectron momentum distribution contains a sum of contributions from different initial states, each of which is a coherent sum of different angular momentum components, making it difficult to decompose the continuum state into individual angular momentum components (*20*–*22*).

Here we preferentially create an almost pure f-wave continuum wave function with $m = 0$ in neon by using an attosecond XUV pulse train synchronized with an infrared (IR) laser pulse through the process of high-harmonic generation. The isolation of the f-wave with $m = 0$ is attributed to the XUV excitation to a resonant bound state that is Stark-shifted by the IR field. By adding an additional coherent pathway that produces an isotropic electron wave, we create a hologram and reveal the alternating sign of the lobes of the f-wave. By controlling the phase of the interfering pathways with attosecond precision, we are able to determine the amplitudes and phases of all six partial-wave components that contribute to the continuum wave function.

The experimental setup is described in detail in the supplementary materials (SM). An 800-nm wavelength laser pulse with a 35-fs duration is focused onto an argon gas jet, producing high-harmonic emission that we label "XUV." In the frequency domain, the emission has peaks at odd-integer multiples of the driving laser frequency. In the time domain, the XUV pulse is composed of a train of attosecond pulses. The high-harmonic emission is focused onto a second gas jet containing neon gas. The neon atoms are excited and photoionized by different high-harmonic orders, and the resulting photoelectrons are recorded by a velocity map–imaging (VMI) spectrometer, which measures their two-dimensional (2D) projection onto a detection plane (*23*). For the phase-resolved measurements, we generate an XUV spectrum that contains both even and odd harmonics, using both 800- and 400-nm driving laser pulses (*24*). In both cases, part of the 800-nm pulse (called "IR") is also focused onto the neon gas, permitting resonant (1 + 1′)-photon, XUV + IR ionization and Stark-shifting of the resonant bound states (*25*). The two-color temporal control and stability of the experiment is <50 as.

We first consider the situation where the XUV is generated by 800 nm only (i.e., no 400-nm contribution). The XUV spectrum then consists of a comb of odd harmonics of the IR driver laser frequency (i.e., no even harmonics). Figure 1A shows the XUV + IR photoelectron momentum distribution for the ionization of neon that is measured under these conditions. At very low momentum, i.e., close to the ionization threshold, a six-fold angular structure is clearly observed. For comparison, an image recorded for helium under the same conditions is shown in Fig. 1B. This experiment may be viewed as the angular-resolved version of a previous study in helium by Swoboda *et al.* (*26*), in which the phase shift due to an intermediate resonance was mapped out. For neon, in Fig. 1A, the outer ring is produced through direct ionization by harmonic 15 (H15), whereas the inner structure results from (1 + 1′)-photon, H13 + IR ionization through the 3d intermediate resonance. The widths in the radial direction of all observed features are a consequence of the frequency bandwidth of the XUV and IR pulses (*27*).

Figure 1C shows an energy level diagram that rationalizes the experimental observations in neon. The XUV photon energy and the IR intensity create a resonance condition for H13 with the Stark-shifted 3d level (see SM). The addition of an IR photon enables (1 + 1′)-photon ionization, producing the central feature seen in Fig. 1A. In Fig. 1C, the atomic eigenstates are labeled with the usual atomic physics notation, i.e., with principal quantum number n and with the orbital angular momentum labeled as s ($\ell = 0$), p ($\ell = 1$), d ($\ell = 2$), and f ($\ell = 3$). A dipole transition between states changes ℓ by ±1. For neon ($1s^2 2s^2 2p^6$), the 2p→3d transition is dipole-allowed, and in the dipole approximation, the continuum electron resulting from XUV + IR ionization must have either p- or f-wave character. We show that the experimental results are consistent with a continuum electron wave function that is predominantly an f-wave with $m = 0$.

The amplitude of the six-fold structure is modulated when the relative delay between the XUV and the IR laser pulses is varied. This modulation is due to the interference between the resonant H13 + IR pathway and the nonresonant H15 – IR pathway (we use the notation H13 + IR and H15 – IR to denote two-photon pathways composed of one harmonic order plus or minus one infrared

[1]National Research Council of Canada, 100 Sussex Drive, Ottawa, ON K1A 0R6, Canada. [2]Joint Attosecond Science Laboratory, National Research Council and University of Ottawa, 100 Sussex Drive, Ottawa, ON K1A 0R6, Canada. [3]Max-Born-Institut, Max Born Straße 2A, D-12489 Berlin, Germany. [4]Fachbereich Physik, Freie Universität Berlin, Arnimallee 14, 14195 Berlin, Germany. [5]Department of Applied Physics, Waseda University, Okubo 3-4-1, Shinjyuku, Tokyo 169-8555, Japan.
***Corresponding author. Email: david.villeneuve@uottawa.ca (D.M.V.); niikura@waseda.jp (H.N.)**

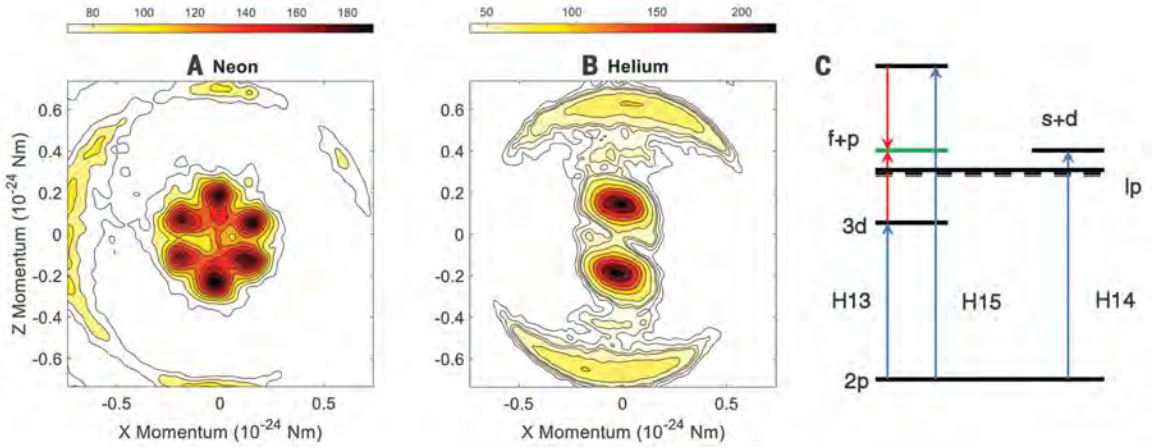

Fig. 1. Experimental velocity-map electron images. The observed photoelectron momentum distributions result from the ionization of (**A**) neon and (**B**) helium by an attosecond pulse train synchronized with the fundamental IR laser pulse. Both pulses were polarized along the vertical (*z*) axis. In both images, the outer rings are due to direct ionization by harmonics 15 (neon) and 17 (helium). The central feature in the neon image results from (1 + 1′)-photon, XUV + IR ionization via the 3d state. The slight left-right asymmetry arises from imperfections in the microchannel plate detector. An energy level diagram in (**C**) shows the levels that are relevant for understanding the neon experiment. The green line labels the six-fold low-energy feature seen in (A).

photon). The SM shows that the phase of the six-fold structure is different from that of the higher-order sidebands, consistent with the occurrence of a phase shift due to the 3d resonance. This result is consistent with the observations of Swoboda *et al.* (*26*) in helium.

Experimentally, the resonant excitation to the Stark-shifted 3d state can be confirmed by measurements of the photoelectron momentum distribution as a function of both the photon energy of the XUV and the IR laser intensity (0 to 4×10^{12} W/cm^2; see SM). At a given XUV photon energy, the six-fold structure is observed when the H13 photon energy matches the 2p→3d resonant energy plus the ponderomotive shift resulting from the IR laser intensity (see SM). However, when the XUV photon energy is larger than the Stark-shifted 2p→3d transition, the six-fold structure disappears into a broad distribution.

The initial 2p state of neon has three orthogonal orbitals, p_x, p_y, and p_z (we consider that in the experiment the laser is polarized along the *z* direction, and the photoelectron is detected in the *xz* plane). Ionization from each initial state should contribute to the final angular distributions. The three components of a continuum f-wave resulting from (1+1′)-photon ionization from the three p orbitals are illustrated in Fig. 2, along with their simulated VMI projections. It is clear that the six-fold structure of Fig. 1A corresponds only to the $m = 0$ case, which is the only orbital that displays the experimentally observed node in the horizontal direction (*x* direction). The dominance of the $m = 0$ channel is both notable and unexpected. Like the ground state, in the absence of the laser field, the $m = 0$ and $m = \pm 1$ components of the 3d resonance are degenerate. Our experiment thus suggests that a Stark shift of the 3d resonant state may be responsible for the selection of the $m = 0$ component. We show in the SM that the Stark shift and ionization rate may be different for $m = 0$ and $m = \pm 1$, causing only the $m = 0$ channel to be shifted into resonance. Figure S5 shows that, for a particular combination of XUV frequency and IR intensity, the contribution of photoelectrons produced through the $m = 0$ channel exceeds by an order of magnitude the contributions from the $m = \pm 1$ channels. This calculation was performed with a 3D time-dependent Schrödinger equation (TDSE) solver by using an effective potential for argon, not neon. As discussed in the SM, this calculation demonstrates the plausibility of $m = 0$ selection by the Stark shift, but the calculation must be done for a benchmarked neon potential.

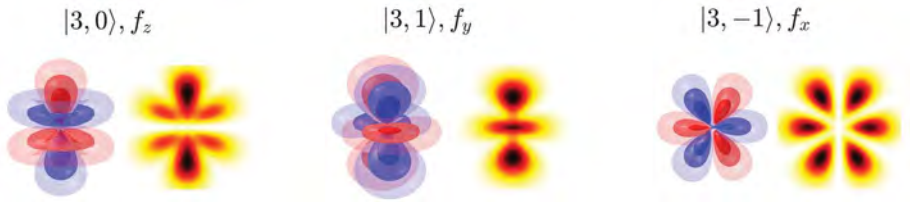

Fig. 2. Calculated continuum wave functions and predicted VMI projections. The individual wave functions for the possible f-wave components are shown to the left of the corresponding projections of the square of the wave function on a 2D plane. Quantization axis is along the vertical (*z*) axis. Only the $m = 0$ case (left) is consistent with the experiment, which always exhibits a node along the horizontal axis. The radial part of the wave functions was simulated with a Gaussian width to correspond to the experimental energy width of the VMI images; the radial information in the experiment is not used—only the angular distributions are used. $f_y = Im(|3,1\rangle + |3,-1\rangle)/\sqrt{2}$ and $f_x = Re(|3,1\rangle - |3,-1\rangle)/\sqrt{2}$.

We next modified the experiment by introducing a third, XUV-only, one-photon pathway to the final continuum state as a homodyne phase reference. Experimentally, this was done by adding the second harmonic of the 800-nm laser pulse to the high-harmonic generation process, resulting in the creation of both even and odd harmonics (*24*). Even-order harmonic H14 creates photoelectrons with the same energy as the H13 + IR and H15 − IR pathways (see Fig. 1C). Direct ionization from the 2p ground state by H14 produces s- and d-waves, which interfere with the predominant f-wave that is created by both (1 + 1′)-photon processes. By varying the relative delay between the XUV and IR pulses, the phases of the XUV + IR, (1 + 1′)-photon processes are altered, whereas the s- and d-waves are unaffected by the delay, providing a constant phase reference for the other channels.

Figure 3 shows measured photoelectron momentum distributions from neon at three different XUV-IR time delays. Compared with Fig. 1A, the lobes in the six-fold angular pattern alternate in intensity, and the intensity distribution is controlled by the XUV-IR delay. The alternating three-fold features can be rationalized in a simple picture by coherently adding an f-wave to an s-wave, or taking their difference, as illustrated in Fig. 3, while neglecting the p- and d-wave components.

The three VMI images shown in Fig. 3A are taken from a series of 100 images recorded at different XUV-IR time delays. These images were

binned into 8° angular sectors, and the counts in each sector were integrated to extract the angular distribution for each image. In Fig. 4A, we plot the observed electron angular distributions of the central structure as a function of the XUV-IR delay. The experimental results are compared to a model in which six possible spherical harmonics are added coherently and then projected onto the xz plane to simulate the VMI images. The total continuum wave function is written as

$$\psi(\theta,\phi) = A_s Y_{00} + A_d e^{i\phi_d} Y_{20} + (A_{p13} e^{i\phi_{p13}} Y_{10} + A_{f13} e^{i\phi_{f13}} Y_{30}) e^{i\omega_0 \tau} + (A_{p15} e^{i\phi_{p15}} Y_{10} + A_{f15} e^{i\phi_{f15}} Y_{30}) e^{-i\omega_0 \tau} \quad (1)$$

where the A's represent amplitudes of each partial wave contribution, ϕ are the corresponding phases, ω is the IR laser frequency, τ is the XUV-IR delay time, and $Y_{\ell m}(\theta,\phi)$ are spherical harmonics. The first two terms of the right side of the equation describe the one-photon ionization by H14 producing s- and d-waves, whereas the latter two terms (containing the dependence on the XUV-IR delay τ) result from the pathway through the 3d resonant state involving H13, and the direct ionization channel involving H15, both producing p- and f-waves. A fit of this model to the experimental data yields the results shown in Fig. 4B; the fitting parameters are listed in Table 1. To ensure that a global optimum was found, we employed a particle swarm optimization algorithm with 10^7 initial conditions. The amplitudes in Table 1 confirm the dominance of the f- and s-wave components over the respective p- and d-wave components that we have used in the discussion of Fig. 3.

As an additional check, we show in the SM that the partial-wave amplitudes and phases in Table 1 are consistent with several further experiments. One is the series of experiments that produced the data shown in Fig. 1A, which were recorded without H14 present; here the equal intensities of all six lobes can only be reproduced when the f- and p-waves are added with the relative phase and amplitude shown in Table 1. In a

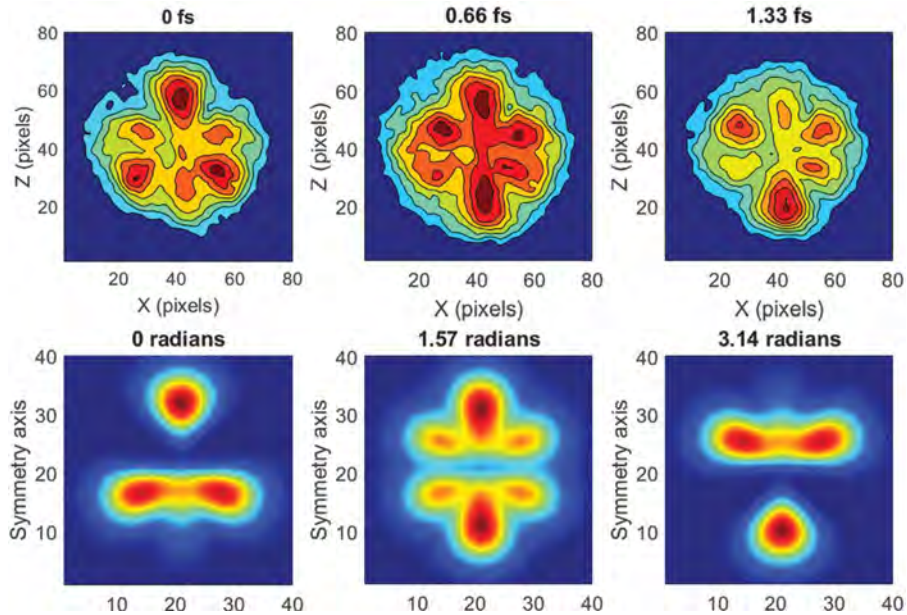

Fig. 3. Electron momentum angular distributions with three pathways. (**Top**) Experimental electron momentum distributions resulting from the ionization of neon via the three pathways (H13, H14, H15) shown in Fig. 1C. The polarization direction is vertical. (**Bottom**) Calculated images for a pure s-wave added to a pure f-wave (m = 0) with equal amplitudes, squared and projected onto a plane, to show that the experimental results are dominated by these two components. For simplicity (and as supported by the data in Table 1), the p- and d-wave contributions are not included. The s-wave component is produced by direct one-photon ionization with H14 and provides a phase reference for the other two interfering pathways. As the phase of the IR pulse is advanced by the times shown above each figure, the phase of the f-wave component is varied. The resulting interference introduces an up-down asymmetry in the momentum distribution that can be controlled by the IR phase.

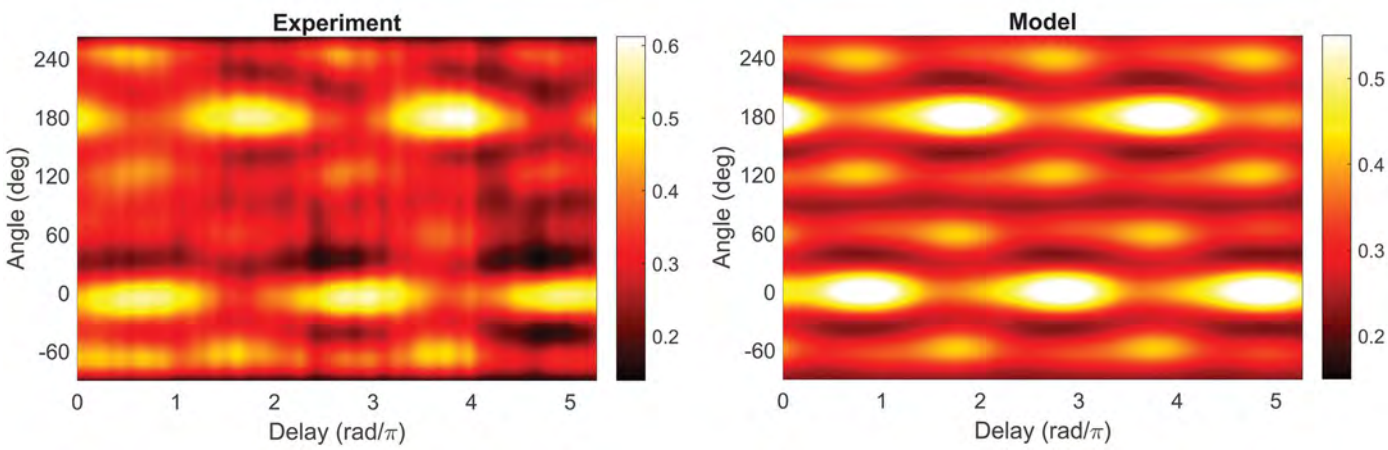

Fig. 4. Angular distribution of the central feature of the VMI images versus XUV-IR delay. Angle zero is defined as the upward direction in the VMI images, parallel to the polarization (z) axis. A delay of π radians corresponds to a delay of half an IR optical period (1.33 fs). (**Left**) Experimental data. (**Right**) Calculated angular distribution based on fitting a 12-parameter model (see Eq. 1) to the experimental data. The amplitudes and phases of each partial wave are listed in Table 1. The dominant pattern is reproduced: Alternating lobes at 0° and 180°, with minor lobes at −60°, 60°, 120°, and 240°. This pattern is associated with the six-fold structure of the dominant f-wave contribution.

Table 1. Parameters of the model fit. The experimental photoelectron angular distributions as a function of XUV-IR delay, shown in Fig. 4A, are fitted to a model composed of six partial waves (see Eq. 1). The amplitudes and phases of each partial wave are listed. The amplitudes are normalized so that the sum of their squares equals one. The phase of the s-wave is defined as zero. ϕ_0 represents an arbitrary common phase that determines time zero. The column labeled "Amplitude^2" is the square of the values in the "Amplitude" column. Errors shown are the range of each parameter such that the residual least-squares error between the model and the experiment increases by 10%.

Fitting parameter	Amplitude	Amplitude^2	Phase (rad)
A_s	$0.83^{+0.04}_{-0.04}$	0.697	0
A_{p13}	$0.16^{+0.05}_{-0.05}$	0.024	$0.54^{+0.41}_{-0.34} + \phi_0$
A_{p15}	$0.15^{+0.05}_{-0.04}$	0.022	$1.93^{+0.41}_{-0.42} - \phi_0$
A_d	$0.10^{+0.05}_{-0.06}$	0.011	$1.57^{+0.30}_{-0.30}$
A_{f13}	$0.32^{+0.04}_{-0.04}$	0.104	$4.16^{+0.19}_{-0.20} + \phi_0$
A_{f15}	$0.39^{+0.03}_{-0.04}$	0.151	$5.04^{+0.16}_{-0.16} - \phi_0$

further experiment, no IR was present, and the inner structure was produced by H14 alone; here the observed angular distribution is in approximate agreement with the relative phase and amplitude of the s- and d-waves in Table 1.

We have shown that, by combining coherent photoionization pathways through a Stark-shifted resonant state, we can create almost pure f-waves with a single magnetic quantum number $m = 0$. The addition of a direct photoionization pathway producing predominantly an s-wave provides a constant phase reference that allows a determination of the phase of the f-wave lobes. By varying the relative phase of the pathways, we can control the direction in which the electrons emanate from the atom, and we can verify the quantum phase of the lobes of the f-wave. We have spatially imaged the angular structure of the continuum wave function and coherently interfered it using a holographic reference composed largely of an isotropic s-wave, leading to the determination of the sign of the quantum wave function. This is a form of coherent control, in which the parity and direction of the electrons can be controlled (*13*, *19*).

In addition, the fitting of a model to the complete experimental data set allows us to determine the exact makeup of the total continuum wave function. In particular, we can determine the amplitude and phase of each partial-wave component. In photoionization parlance, this is a "complete" experiment (*20*).

We have implemented a number of novel approaches, such as a sophisticated two-color interference experiment with careful use of both even and odd harmonics and the use of Stark-tuning to include or exclude desired quantum pathways. These new tools in the attosecond toolbox may allow us to study more complex systems. For example, can we apply a similar approach to a molecule? By exploiting rotational wave packets, will it be possible to determine both the amplitude and phase of transition moments in the molecular frame?

If the photon energy of the XUV can be tuned widely to select a particular intermediate quantum state, our method allows the measurement of phase-resolved orbital images of other states and in different atoms. For instance, if the electron is excited from a lower-lying level to a doubly excited state, dynamical changes in the amplitude and phase resulting from electron correlation can be imaged directly with attosecond time resolution.

REFERENCES AND NOTES

1. H. Wimmel, *Quantum Physics and Observed Reality: A Critical Interpretation of Quantum Mechanics* (World Scientific, Singapore, 1992).
2. A. S. Stodolna *et al.*, *Phys. Rev. Lett.* **110**, 213001 (2013).
3. H. Niikura *et al.*, *Nature* **417**, 917–922 (2002).
4. J. Itatani *et al.*, *Nature* **432**, 867–871 (2004).
5. S. Haessler *et al.*, *Nat. Phys.* **6**, 200–206 (2010).
6. P. M. Kraus *et al.*, *Science* **350**, 790–795 (2015).
7. M. Meckel *et al.*, *Science* **320**, 1478–1482 (2008).
8. M. Meckel *et al.*, *Nat. Phys.* **10**, 594–600 (2014).
9. D. Ray *et al.*, *Phys. Rev. Lett.* **100**, 143002 (2008).
10. V. Gruson *et al.*, *Science* **354**, 734–738 (2016).
11. S. Haessler *et al.*, *Phys. Rev. A* **80**, 011404 (2009).
12. K. T. Kim *et al.*, *Phys. Rev. Lett.* **108**, 093001 (2012).
13. G. Laurent *et al.*, *Phys. Rev. Lett.* **109**, 083001 (2012).
14. J. Mauritsson *et al.*, *Phys. Rev. Lett.* **105**, 053001 (2010).
15. T. Remetter *et al.*, *Nat. Phys.* **2**, 323–326 (2006).
16. A. Rouzée *et al.*, *J. Phys. At. Mol. Opt. Phys.* **47**, 124017 (2014).
17. J. Cooper, R. N. Zare, *J. Chem. Phys.* **48**, 942–943 (1968).
18. J. Cooper, R. N. Zare, in *Atomic Collision Processes*, G. Geltman, K. T. Mahanthappa, W. E. Brittin, Eds. (Lectures in Theoretical Physics, Gordon and Breach, 1969), vol. XIc, pp. 317–337.
19. Y.-Y. Yin, C. Chen, D. S. Elliott, A. V. Smith, *Phys. Rev. Lett.* **69**, 2353–2356 (1992).
20. U. Becker, *J. Electron Spectrosc. Relat. Phenom.* **96**, 105–115 (1998).
21. J. C. Hansen, J. A. Duncanson, R.-L. Chien, R. S. Berry, *Phys. Rev. A* **21**, 222–233 (1980).
22. K. L. Reid, *Annu. Rev. Phys. Chem.* **54**, 397–424 (2003).
23. A. T. J. B. Eppink, D. H. Parker, *Rev. Sci. Instrum.* **68**, 3477–3484 (1997).
24. N. Dudovich *et al.*, *Nat. Phys.* **2**, 781–786 (2006).
25. E. B. Saloman, C. J. Sansonetti, *J. Phys. Chem. Ref. Data* **33**, 1113–1158 (2004).
26. M. Swoboda *et al.*, *Phys. Rev. Lett.* **104**, 103003 (2010).
27. N. Dudovich, D. Oron, Y. Silberberg, *Phys. Rev. Lett.* **88**, 123004 (2002).

ACKNOWLEDGMENTS

The authors gratefully acknowledge discussions with T. Morishita, A. Stolow, M. Ivanov, I. Tamblyn, and A. Korobenko, as well as funding from the Japan Society for the Promotion of Science (JSPS) Grants-in-Aid for Scientific Research (KAKENHI) grant no. 25247069. Data are available upon request from david.villeneuve@uottawa.ca.

SUPPLEMENTARY MATERIALS

www.sciencemag.org/content/356/6343/1150/suppl/DC1
Materials and Methods
Figs. S1 to S8
Table S1
References (*28*–*32*)

23 January 2017; accepted 3 May 2017
10.1126/science.aam8393